Pergamon

Int. J. Heat Mass Transfer. Vol. 39, No. 16, pp. 3347–3355, 1996

0017-9310/96 $15.00+0.00

PII: S0017-9310(96)00009-9

Experimental observation of interface shapes in the float zone of lithium niobate during a CO_2 laser melting

CHIEH HU and JYH-CHEN CHEN

Department of Mechanical Engineering, National Central University, Chung-Li, Taiwan 32054, Republic of China

(*Received* 8 *August* 1995 *and in final form* 26 *December* 1995)

Abstract—The radiosity from a rod of lithium niobate that was heated uniformly by a CO_2 laser with an axisymmetric ring-shaped beam was measured by a two-dimensional infrared imaging radiometer with bandpass filters chosen to be 3–5, 8–12, and 10.6 μm. The radiative characteristics of the volumetric emission and the significant difference of the emitted thermal radiation between the solid or melt and background for wavelengths of 3–5 μm was used to determine the interface shapes of the float zone during the CO_2 laser melting process. The trend of the power distribution impinging on the rod surface may be deduced from the reflection of the CO_2 laser. The gas bubbles existing in the melt may also be monitored. The surface temperature was determined from the distribution of the radiosity for wavelengths of 8–12 μm. The surface temperature distribution is modified significantly be thermocapillary convection. With an increase of the input power, the gas–melt interface changes from concave towards the melt to convex at the upper zone and concave at the lower zone due to the effect of gravity. Copyright © 1996 Elsevier Science Ltd.

1. INTRODUCTION

It is well known that the interface shapes and the transport phenomena in the melt play an important role during the float-zone crystal growth process. The shape of the melt–solid interface affects the distribution of defects in the resultant crystals [1, 2]. When the melt–solid interface is convex to the melt, line defects propagate towards the edge of the crystal rod. Conversely, if the melt–solid interface is concave to the melt, the defects are concentrated at the center of the resultant crystals. The external shape of the resultant crystal relates to the shape of the gas–melt interface at the solid–liquid–vapor junction during the growth [3]. The striations in the crystals are believed to result from thermocapillary-convection instability in the melt during growth [4]. Therefore, in order to obtain high-quality crystals, it is necessary to better understand and control the transport phenomena and the interface shapes.

It is difficult to detect the shapes and the transport phenomena during a crystal growth because the melting point of most crystal materials exceeds 1000°K, and the melt is incandescent. To understand the heat and flow transports in the float-zone system, many investigators have simulated the float zone by a liquid bridge held between two concentric, cylindrical rods. In this model experiment, low melting point fluids with higher Prandtl number ($Pr > 1$) are used, and the heating conditions and zone length can be selected independently. The flow behavior can be detected by measuring temperature inside the bridge or using the light cut technique [5, 6]. In the real float-zone process the heat and flow transports and the interface shapes are strongly coupled, especially for higher Prandtl materials [7–9]. In the float-zone system, the molten zone may be distorted by the capillary force between the thermocouple and the float zone. It is usually suggested to monitor the temperature distribution of the thermal system with a radiometer. However, thermal radiometer measurement is stili hindered by the unknown radiative properties at such high temperatures, which are difficult to measure. In general, the shape of the melt–solid interface during a melt-growth process is usually observed from the shape of growth striations in the interior of the resultant crystals [1, 10, 11].

In recent years, the CO_2 laser-heated float-zone growth technique [12] has been successful in growing single crystals of refractory oxides. Refractory oxides have high transparency in the spectrum between the short-wavelength absorption edge in the ultraviolet region and the long-wavelength absorption edge in the infrared region, and they very quickly become opaque past the long-wavelength absorption edge. They also have small reflectivity in the spectrum before the onset of the Reststrahlen band [13, 14]. Therefore, refractory oxides have low reflectivity and high absorption at the spectrum between the long-wavelength absorption edge and the start of the Reststrahlen band.

For most refractory oxides, a wavelength of 10.6 μm is located in this region. This is why refractory oxides efficiently absorb a CO_2 laser with a wavelength

NOMENCLATURE

D	diameter of the material rod [mm]	z	the axial coordinate [mm].
I	intensity of the output voltage [arb.]	Greek symbols	
Lc_u	inner zone length of the upper zone	α	thermal diffusivity [$m^2 s^{-1}$]
Lc_l	inner zone length of the lower zone	ν	kinematic viscosity [$m^2 s^{-1}$]
Ls_u	outer zone length of the upper zone	ρ_l	density of the liquid phase of the $LiNbO_3$ [g cm^{-3}]
Ls_l	outer zone length of the lower zone	ρ_s	density of the solid phase of the $LiNbO_3$ [g cm^{-3}]
P	reference input laser power [mW]	θ_u	upper contact angle [degree]
Pr	$= \nu/\alpha$ Prandtl number	θ_l	lower contact angle [degree].
T	temperature [°C]		

near 10.6 μm. Recently, Chen and Hu [15, 16] used a thermal imaging radiometer to measure the thermal radiation emitted from the heating region of a rod of lithium niobate ($LiNbO_3$), a refractory oxide, in a CO_2 laser-heated float-zone process. They showed that the thermal radiation emitted from a small $LiNbO_3$ rod in the 3–5 μm spectrum is a volumetric phenomenon, and the emittances of the solid and melt are significantly different. Thermal emission in the 8–12 μm is a surface phenomenon, and the emissivity is very high and near unity. The emissivity for the wavelengths of 10.6 and 8–12 μm is insensitive to the variation of the temperature. They used these thermal radiative characteristics to develop a new technique to detect the location of the melt–solid, gas–melt–solid interfaces and measure the surface temperature during the float-zone process. In their technique, the location of the interfaces is determined through the significant change of the emitted thermal radiation intensity in the 3–5 μm spectrum at the interface. The melt–solid interface determined by this model is consistent with those observed from the interior structure of the resolidification rod [15]. Because the temperature at the gas–melt–solid interface is the melting point of the material, the surface temperature distribution can be determined from the thermal radiation emission in the 8–12 μm spectrum using the Planck radiation law.

In this study, we will extend the technique developed by Chen and Hu [15, 16] to monitor the variation of the interface shapes and the surface temperature of a $LiNbO_3$ rod with respect the input power during a CO_2 laser-heated float-zone melting process. The heat and fluid transports are predicted according to the interface shape and the distribution of the surface temperature.

2. EXPERIMENTAL TECHNIQUE

The schematic diagram of the experimental apparatus is illustrated in Fig. 1. As shown in this figure, a cylindrical rod of $LiNbO_3$ is melted by a 50 W continuous waveguide CO_2 laser (Edinburgh, model PL5). The solid beam diameter of the CO_2 laser at the output coupler is 7.5 mm, with a divergence of 2 milliradians. The CO_2 laser is operating at a wavelength of 10.6 μm. The magnitude of the laser power impinging the surface of the material rod is controlled by the size of the iris diaphragm. A beam splitter is used to split about 10% of the laser's power into the power meter to record power variations. The solid beam is transferred into an axisymmetric ring-shaped beam by axicon optics working with reflectors and mirrors. The axicon optics consist of a meniscus lens and an axicon component which produces a converging ring beam as the primary beam passes. The effective focus length of meniscus lens is 135 mm and the deviation angle of the axicon component is 15°. As shown in Fig. 1, the ring-shaped beam is not impinging on the rod surface in the normal direction.

The $LiNbO_3$ rod is fabricated from polycrystalline powders by a pressing and sintering processes. Since the interior structure of the rod is porous, the density of the present $LiNbO_3$ rod measured by the Archimedes principle is around 4.1 g cm^{-3}, and it is less than the density for a single crystal ($\rho_s = 4.6437$ g cm^{-3}). A diameter of 1.5 mm for the porous rod is selected, with a length of 30 mm. The rod of $LiNbO_3$ is heated by stepwise increases of the laser power. No crystals are grown in the present experiments. For a specific input power, the energy used to heat a small portion of the rod is dissipated from the rod surface by convection and thermal radiation. The radiosity from the heating area of the cylindrical rod is measured by an infrared two-dimensional imaging radiometer (Inframatrics, model 760), which views the rod surface normally. During the melting process, three bandpass filters have been switched simultaneously to record the radiosity at wavelengths of 3–5, 8–12 and 10.6 μm. To enhance the spatial resolution of the measurement, a 3× telescope and close-up lens are mounted on the radiometer system. The intensity of the output voltage, I, from the thermal radiometer represents the intensity of the radiation. Noise is eliminated by a 20th order lowpass digital Butterworth filter with a cutoff frequency of 75 Hz.

Based on the method developed by Chen and Hu

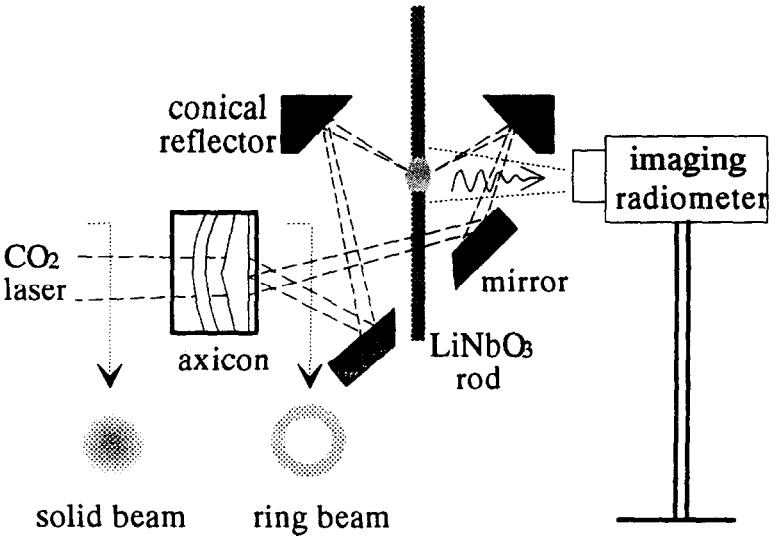

Fig. 1. Schematic diagram of the float-zone system.

[15], the thermal emission for wavelengths of 3–5 μm can be used to determine the variation of the interfaces during the melting process. Chen and Hu [16] have already shown that if a molten zone is formed, the interference of CO_2 laser on the thermal emission for wavelengths of 8–12, and 10.6 μm can be minimized owing to the optically smooth surface of the deformable gas–melt interface and the directional radiation of the laser. Therefore, when the surface zone length of the melt is greater than the laser heating width, the axial temperature distribution can be obtained from the thermal radiation distribution for wavelengths of 8–12 and 10.6 μm using Planck's law [16]. From the numerical results [7], we know that the temperature in the solid region is almost independent of the radial direction and that it varies significantly in the axial direction. Hence, we can obtain the relationship between the intensity of emitted thermal radiation for wavelengths of 3–5 μm and that for a wavelength of 10.6 μm for a specific temperature in the solid region. When the rod is unmelted, the radiosity for wavelengths of 8–12 and 10.6 μm includes the diffuse reflection of the CO_2 laser and the thermal emission from the heating rod. Based on the results for 3–5 μm, and the relationship of the thermal emission for wavelengths between the 3–5 and 10.6 μm, the thermal emission from the rod surface at the spectrum of 10.6 μm may be calculated. Therefore, if the rod is unmelted, the reflection intensity of the CO_2 laser can be determined after we remove the thermal emission of the rod from the radiosity for a wavelength of 10.6 μm. A typical result obtained by this process illustrated by Fig. 2. It is clear that the distribution of the reflection of the CO_2 laser in the axial direction is similar to a Gaussian distribution. There exists, however, a small tail at the upper side. According to this result, we expect that the laser power in the axial direction impinging on a rod surface near a Gaussian distribution with an upper tail. The ring pattern measured by Belanger and Rioux [17] also exhibits this characteristic. From Fig. 2, we can see that the heat center, which has the maximum intensity of laser power, is located at $z = 5.1$ mm, and 95% of the laser power is concentrated within a region with a width of 3.5 mm.

3. RESULTS AND DISCUSSION

The reference laser input power, P, represents the energy detected by the power meter. Figure 3 displays the thermal radiographs for wavelengths of 3–5 μm with four different powers. Figure 4 shows the zone shapes for four different powers corresponding to Fig. 3, determined by using the technique developed by Chen and Hu [15]. Since the density for the melt ($\rho_l = 3.64$ g cm^{-3}) is less than that for the porous solid, the volume of the float zone is greater than that of the solid corresponding the float zone before melting, a requirement needed to satisfy the conservation of mass. Therefore, for smaller powers [Fig. 4(a, b)], the results show that the shape of the deformable gas–melt interface is concave to the melt. For larger powers [Fig. 4(c, d)], the shape of the gas–melt interface becomes convex towards the melt at the upper zone and concave towards the melt at the lower zone, due to the effect of gravity. Recent numerical computations performed by Chen and Hu [18] showed that in a zero gravity environment the gas–melt interface is always concave to the melt. From Fig. 4, it is obvious that the zone length increases with an increase of the input CO_2 laser power, and the melt–solid interface is always convex to the melt.

Since the structure of the solid rod is porous, we expect that the gas bubble will be nucleated on the solid–melt interface during the melting and that the size of the bubble will grow when more solid is melted. When the gas bubble appears in the melt, it may be seen clearly from the isothermal radiograph due to

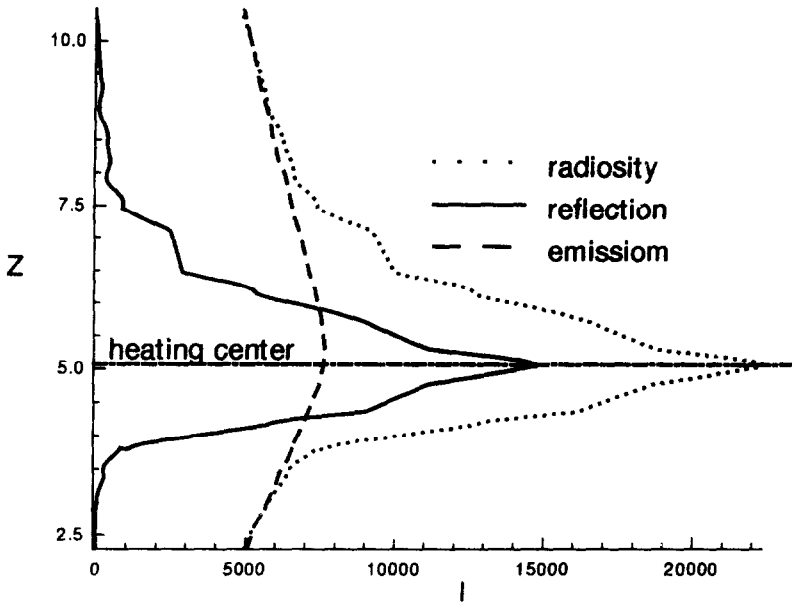

Fig. 2. Distribution of the reflection intensity of the CO_2 laser in the axial direction for $P = 290$ mW.

the significant variation of the radiation intensity around the gas bubble (Fig. 3). The thermal radiographs in Fig. 3 are taken after the input power has been maintained at a particular value with less 3% deviation for a certain period of time. The gas bubbles appearing in Fig. 3 are at rest. In Fig. 3(a) ($P = 530$ mW), we can see that a gas bubble appears in the upper part of the isothermal radiograph. Actually, the position is located at the right corner of the melt–solid interface of the upper zone [Fig. 4(a)]. For $P = 560$ mW, a new gas bubble appears near the melt–solid interface of the lower zone, and the gas bubble in the upper zone grows much larger [Fig. 4(b)]. Three gas bubbles are detected in the melt for $P = 590$ mW [Fig. 4(c)], and two gas bubbles are monitored for $P = 650$ mW. Figure 4 only shows the axial position of the bubbles: the depth is still unknown because they are obtained from a two-dimensional thermal radiograph. In Fig. 4, the gas bubbles are motionless due to the balance of the buoyancy force, the thermocapillary migration force, and the inertial force generated by the thermocapillary flow in the melt. The buoyancy force will push the bubble upward. The bubble will move towards the higher temperature region of the fluid due to the thermocapillary migration force [19]. Therefore, the thermocapillary migration force will move the bubble downward in the upper zone and upward in the lower zone. The thermocapillary flow in the melt is induced by the surface tension gradients at the gas–melt interface. According to the results of a numerical simulation [18], there are two toroidal cells in the melt. The flow motion confined to a small region near the gas–melt interface is moving toward the melting solid interface where it starts sinking. Near the core it is moving away from the melt–solid interface, and near the heating center it is rising up. Therefore, the inertia force induced by the thermocapillary flow will push the gas bubble towards the melt–solid interface when the gas bubble appears near the gas–melt interface. By contrast, the inertia force generated by the thermocapillary flow will move the gas bubble away from the melt–solid interface when the gas bubble appears near the core. When the bubble appears near the core at the lower zone, it may shift to a position near the center of the toroidal cell and then follow the flow motion of the vortex. This occurs when the thermocapillary convection is strong enough (higher input power). For smaller input power ($P < 670$ mW), we do not observe that the gas bubble is moving with the thermocapillary flow. The gas bubble moving with the flow of the vortex has been detected in the lower zone for higher input power ($P > 670$ mW) by the present experiment. The velocity of the bubble is about 20 mm s^{-1}. Chu [20] has computed the velocity of thermocapillary flow in the $LiNbO_3$ melt. The bubble velocity observed by the present experiments is very close to the magnitude of the surface velocity computed by Chu. The gas bubble in the upper zone stays at the position near the melt–solid interface, and its size increases with an increase of the input power due to the merging of the bubbles.

When the surface zone length in the melt exceeds the mostly incident width of the laser beam, the interference of the laser reflection is significantly reduced, and the method developed by Chen and Hu [16] is used to determine the surface temperature distribution along the longitudinal direction. Figure 5 displays the surface temperature in the longitudinal direction for three different powers. The results show that the maximum temperature occurs at the position near the heating center of the laser power ($z = 5.1$ mm). It is obvious that the surface temperature decreases slowly

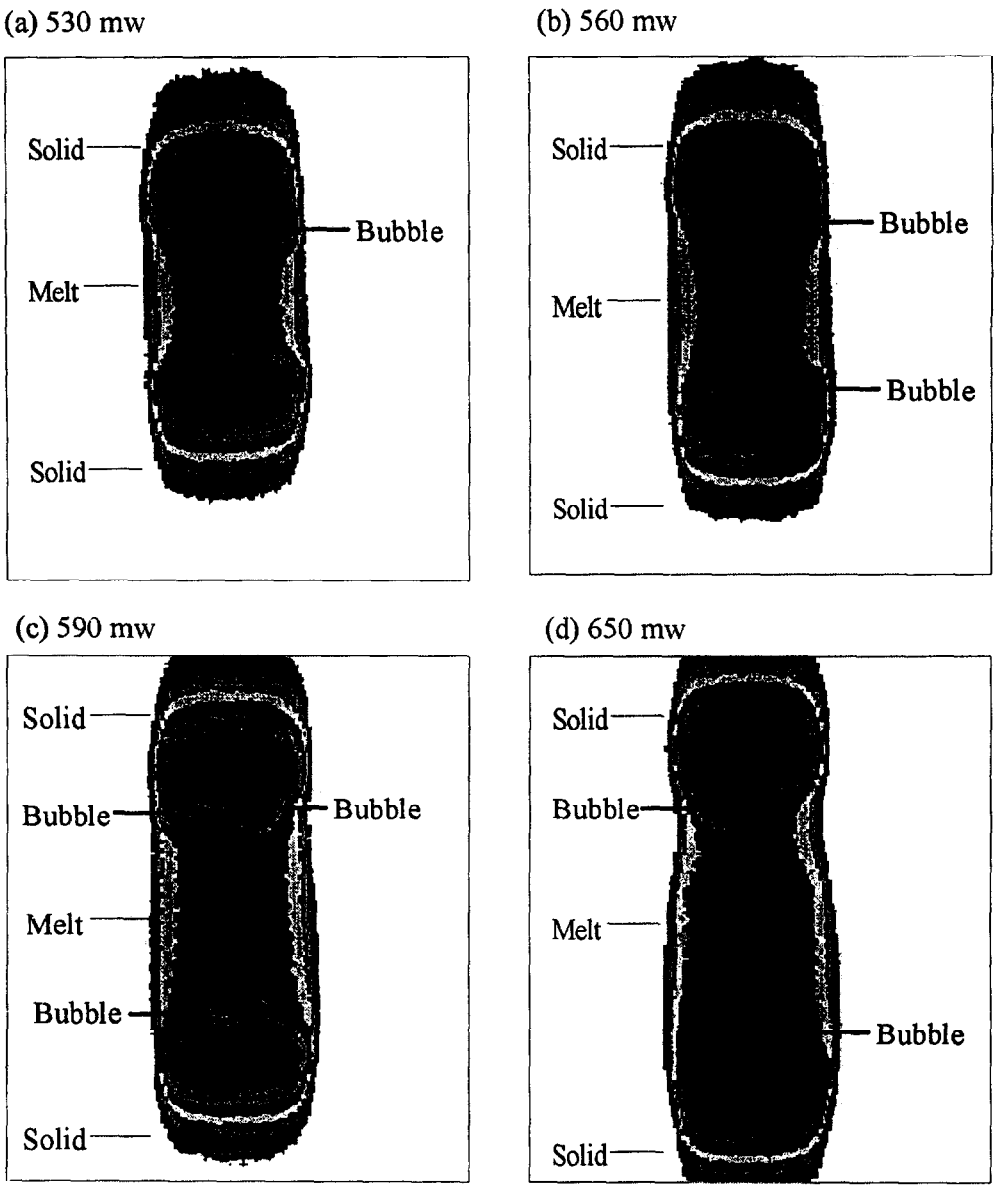

Fig. 3. Thermal radiographs for wavelengths in the range of 3–5 μm with four different P.

away from the position with the maximum surface temperature, and it decreases significantly when the position is close to the gas–melt–solid interface. Numerical simulations [7, 8] have shown that for smaller Prandtl melts the temperature distribution is mainly determined by the thermal diffusion, while for higher Prandtl melts the temperature in the melt is modified significantly by the axial energy induced by the thermocapillary flow. For higher Prandtl melts, since the energy is transferred to the melt–solid interface by the stronger momentum transport, an increase of the input energy is mainly employed to enlarge the size of the float zone. Only a small part of the input energy is converted into the internal energy of the melt. The Prandtl number of the $LiNbO_3$ melt is around 55. This is why in Fig. 5 the increase of the zone length is more significant than that of the maximum temperature as the input power increases. From Fig. 4, we see that when the input power increases, the shape of the gas–melt interface changes from concave towards the melt to convex at the upper zone and concave at the lower zone due to the influence of gravity. It is obvious that the force of gravity depresses the size of the cross-section area of the upper zone and enhances that of the lower zone. The amount of the heat transfer in the axial direction is proportional to the size of the cross-section area. Therefore, the heat transport in the axial direction for the upper zone is much less than that for the lower zone, due to the influence of the gas–melt interface shape. This is why in Fig. 5 the increase rate of the upper zone is slower than that of the lower zone.

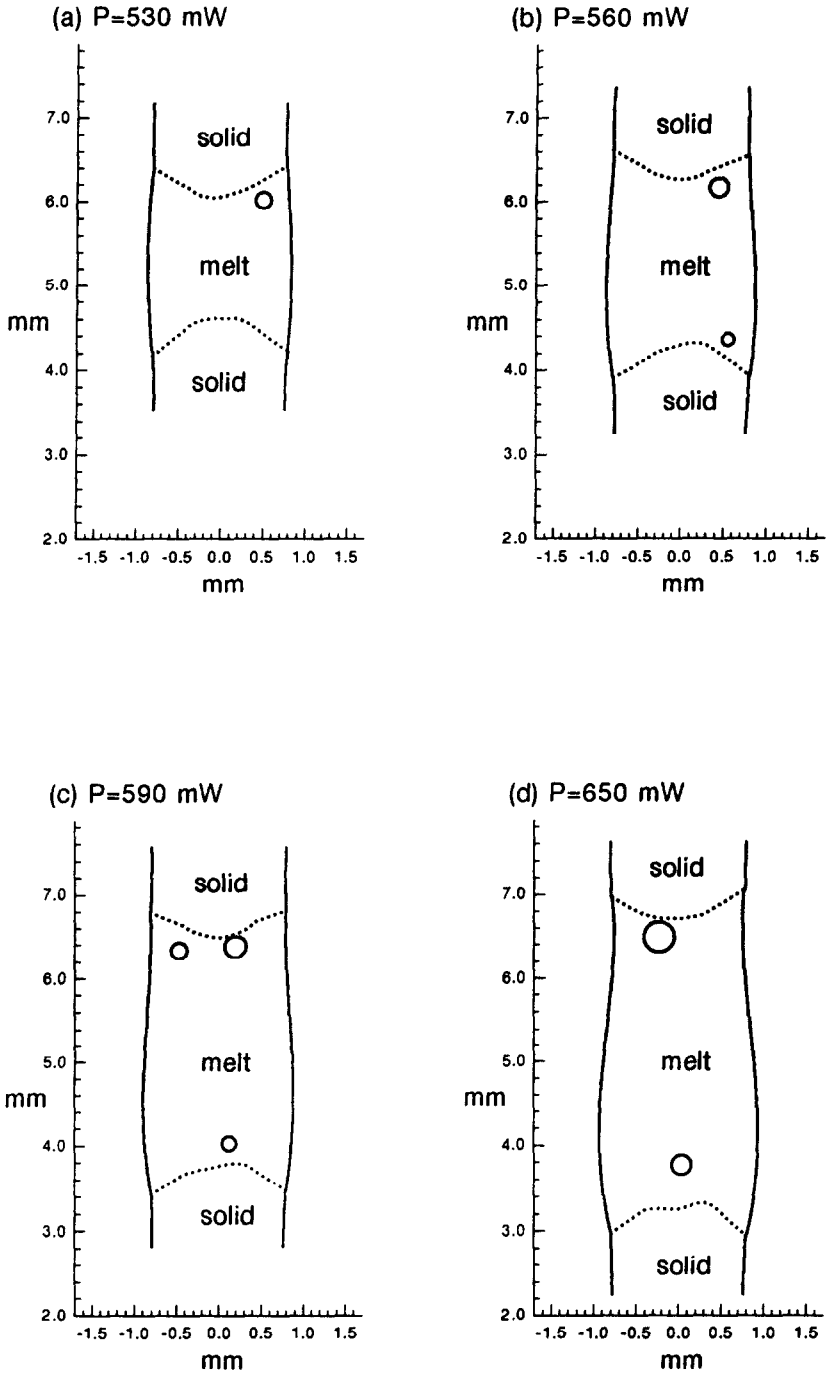

Fig. 4. Zone shape determined from the variation of the emitted intensity of thermal radiation for wavelengths of 3–5 μm with four different P.

We use Ls_u, Lc_u, Ls_l and Lc_l, to represent the outer and inner zone lengths above the heating center and below the heating center, respectively. Figure 6 shows the variation of the upper and lower zone lengths with the reference input laser power. From Fig. 2, we can conjecture that the input laser power for the upper zone is larger than that for the lower zone. Therefore, when the float is formed, the upper zone length is longer than the lower zone length. The results of the numerical simulation performed by Chen and Wu [18] showed that for smaller input power the upper zone length is very close to the lower one, since the power distribution used is symmetric at the heating center and the effect of gravity is still small. In Fig. 6, with the increase of the input laser power, the increase rate of the lower zone length is faster than that of the upper zone due to the influence of the deformation of the gas–melt interface induced by gravity. The numeri-

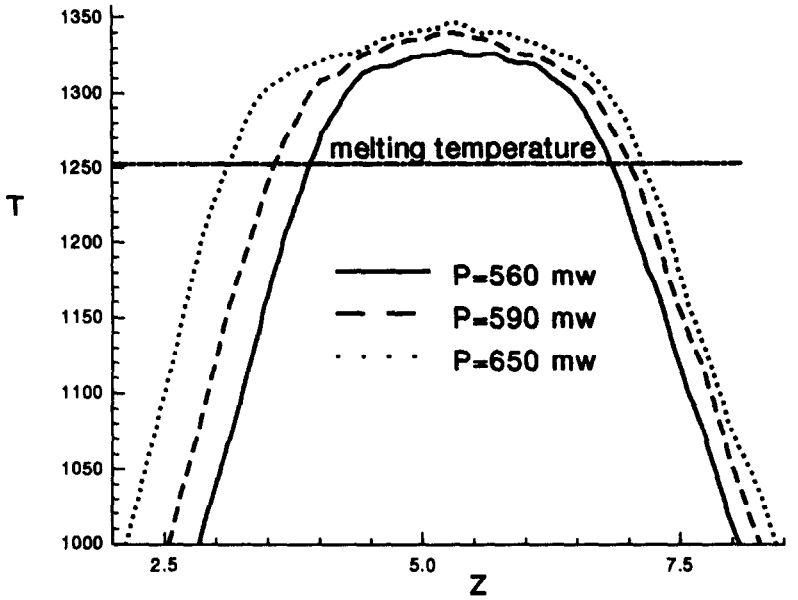

Fig. 5. Surface temperature distribution in the axial direction for three different P.

cal results also reflect this trend. When $P > 600$ mW, the lower zone length becomes greater than the upper zone length. For $P > 700$ mW, the float zone breaks down. The surface zone length for $P = 700$ mW is about 4.5 mm. Figure 6 shows that the melt–solid interface is convex to the melt because the outer zone length is always greater than the inner zone length. The difference of the outer and the inner zone lengths does not vary significantly with the variation of the input laser power.

The contact angle is defined as the angle between the tangent to the gas–melt interface at the gas–melt–solid trijunction and the axis of the rod. We used θ_u and θ_l to denote the contact angles of the upper and lower zones, respectively. Figure 7 illustrates the variation of the upper and lower contact angles with respect to the reference input laser power. The upper contact angle is smaller than the lower one due to the influence of gravity. For small input powers ($P < 540$ mW), the difference is not significant. The discrepancy increases with the increase of the input laser power, since the influence of gravity increases with an increase of the length of the float zone. The value of the lower contact angle is always positive, and the upper contact angle changes from positive to negative at $P \approx 590$ mW. It is obvious that the gas–melt interface changes

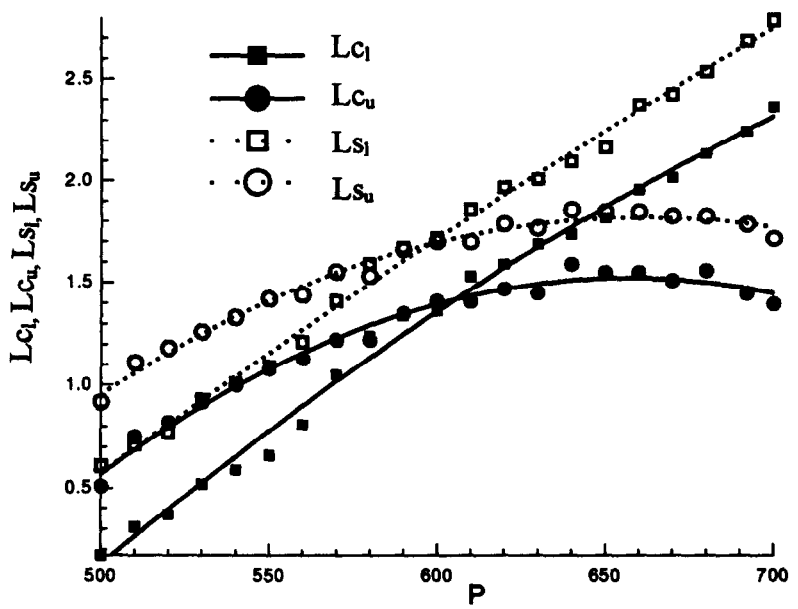

Fig. 6. Outer and inner lengths of the upper and lower zones vs reference input laser power P.

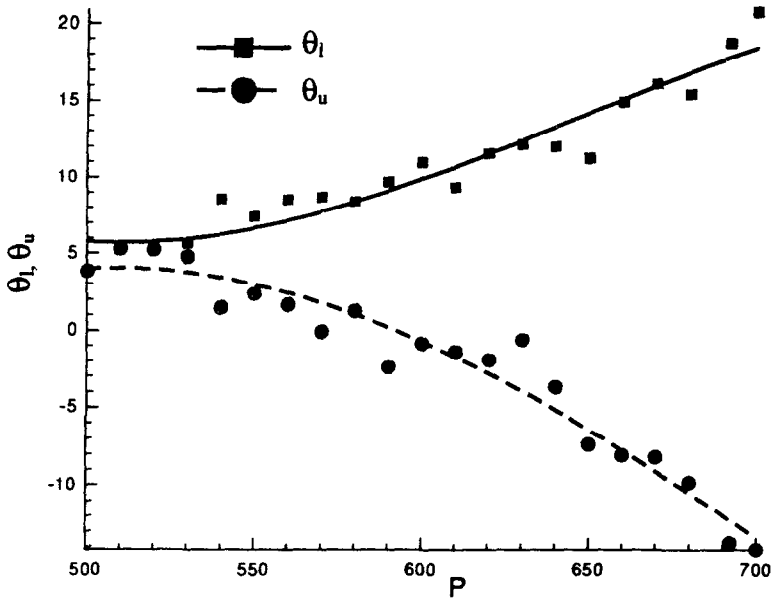

Fig. 7. Contact angle vs reference input laser power P.

from concave towards the melt to convex at the upper zone and concave at the lower zone when the laser power exceeds 590 mW.

4. CONCLUSION

In the present study, the variation of the interface shapes of the float zone for $LiNbO_3$ with the input CO_2 laser power is investigated using the method developed by Chen and Hu [15]. The results show that the melt–solid interface is always convex to the melt. For smaller input powers, the gas–melt interface is concave to the melt. For higher input powers, the gas–melt interface becomes convex at the upper zone and concave at the lower zone owing to the effect of gravity. The presence of a gas bubble in the melt may be detected. The gas bubble is driven by the buoyancy force, the thermocapillary migration force, and the thermocapillary flow generated by the surface tension gradients due to the nonuniform temperature distribution along the gas–melt interface. In our observations, the gas bubble in the lower zone may drift upward into the upper zone or move to a location near the center of the vortex in the lower zone and follow the motion of the thermocapillary flow. The contact angle of the upper zone is smaller than that of the lower zone due to the effect of gravity. When the input power increases, the value of the lower contact angle increases, and that of the upper contact angle decreases and changes from positive to negative.

It is a trivial problem to use the radiation characteristics to determine the interface shapes and the temperature distribution of the float zone for $LiNbO_3$ during a melting process. We also expect that this technique can be extended to study other refractory materials.

Acknowledgements—The authors gratefully acknowledge the support of the National Science Council of Taiwan, Republic of China for this work through grant no. NSC 83-0401-E008-004.

REFERENCES

1. K. Kitamura, S. Kimura and S. Hosoya, The interface shapes of some oxide materials grown by the floating zone method, *J. Crystal Growth* **48,** 469–472 (1980).
2. J. C. Chen, Y. C. Lee and C. Hu, A simple method to understand the propagation of defects in the floating-zone solidification process of lithium niobate, *the Eleventh International Conference on Crystal Growth.* (1995).
3. T. Surek, Theory of shape stability in crystal growth from the melt, *J. Appl. Phys.* **47,** 4384–4393 (1976).
4. M. Jurisch and W. Loser, Analysis of periodic non-rotational *W* striations in Mo single crystals due to non-steady thermocapillary convection, *J. Crystal Growth* **71,** 214–222 (1990).
5. C. H. Chun, Marangoni convection in a floating zone under reduced gravity, *J. Crystal Growth* **48,** 600–610 (1980).
6. F. Preisser, D. Schwabe and A. Scharmann, Steady and oscillatory thermocapillary convection in liquid columns with free cylindrical surface, *J. Fluid Mech* **126,** 545–567 (1983).
7. J. C. Chen, C. F. Chu and W. F. Ueng, Thermocapillary convection and melt–solid interface in the floating zone, *Int. J. Heat Mass Transfer* **37,** 1733–1748 (1994).
8. J. C. Chen and C. F. Chu, Numerical computation of fluid flow of floating-zone crystal growth of molybdenum, *Int. J. Heat Mass Transfer* **38,** 1841–1853 (1995).
9. J. C. Chen and G. H. Chin, Linear stability analysis of thermocapillary convection in the floating zone, *J. Crystal Growth*, **154,** 98–197 (1995).
10. A. Hirata, M. Tachibana, T. Sugimoto, Y. Okano and T. Fukada, Control of crystal-melt interface shape during growth of lithium niobate single crystal, *J. Crystal Growth* **131,** 145–152 (1993).
11. J. Trauth and B. C. Crabmajer, the shape of the crystal/melt interface during the growth of lithium niobate crystals by the Czochralski technique, *J. Crystal Growth* **112,** 451–457 (1991).

12. R. S. Feigelson, Pulling optical fibers, *J. Crystal Growth* **79,** 669–681 (1986).
13. J. R. Jasperse, A. Kahan, J. N. Plendl and S. S. Mitra, Temperature dependence of infrared dispersion in ionic crystals LiF and MgO, *Phys. Rev.* **146,** 526–542 (1966).
14. A. S. Barker Jr and R. Loudon, Dielectric properties and optical phonons in $LiNbO_3$, *Phys. Rev.* **158,** 433–445 (1967).
15. J. C. Chen and C. Hu, Measurement of the float-zone interface shape for lithium niobate, *J. Crystal Growth* **149,** 87–95 (1995).
16. J. C. Chen and C. Hu, Measurement of the surface temperature in the float zone of $LiNbO_3$, *J. Crystal Growth* **158,** 289–295 (1996).
17. P. A. Belanger and M. Rioux, Ring pattern of a lens-axicon doublet illuminated by a Gaussian beam, *Appl. Opt.* **17,** 1080–1086 (1978).
18. J. C. Chen and H. K. Wu, Numerical computation of heat flow, fluid flow and interface shapes in the float zone of lithium niobate during a melting process, *Int. J. Heat Mass Transfer* (in press).
19. N. O. Young, J. S. Goldstein and M. J. Block, The motion of bubbles in a vertical temperature gradient, *J. Fluid Mech.* **6,** 350–356 (1959).
20. C. F. Chu, Velocity and temperature distributions in the floating zone, Master thesis, National Central University, Chung-Li, Taiwan (1994).